

Article

# Band Gap Modulation of Tantalum(V) Perovskite Semiconductors by Anion Control

Young-Il Kim <sup>1,2,\*</sup>  and Patrick M. Woodward <sup>2</sup><sup>1</sup> Department of Chemistry, Yeungnam University, Gyeongsan 38541, Korea<sup>2</sup> Department of Chemistry and Biochemistry, The Ohio State University, Columbus, OH 43210, USA; woodward.55@osu.edu

\* Correspondence: yikim@ynu.ac.kr; Tel.: +82-53-810-2353

Received: 11 January 2019; Accepted: 3 February 2019; Published: 7 February 2019



**Abstract:** Band gap magnitudes and valence band energies of Ta<sup>5+</sup> containing simple perovskites (BaTaO<sub>2</sub>N, SrTaO<sub>2</sub>N, CaTaO<sub>2</sub>N, KTaO<sub>3</sub>, NaTaO<sub>3</sub>, and TaO<sub>2</sub>F) were studied by diffuse reflection absorbance measurements, density-functional theoretical calculations, and X-ray photoelectron spectroscopy. As a universal trend, the oxynitrides have wider valence bands and narrower band gaps than isostructural oxides, owing to the N 2*p* contribution to the electronic structure. Visible light-driven water splitting was achieved by using Pt-loaded CaTaO<sub>2</sub>N, together with a sacrificial agent CH<sub>3</sub>OH.

**Keywords:** perovskite oxynitride; band gap; density-functional theory; water splitting

## 1. Introduction

Transition metal oxynitrides are of interest due to their potential as photocatalysts [1–6], pigments [7,8], battery electrodes [9], high-permittivity dielectrics [10], etc. Such a diverse functionality of oxynitrides is derived largely from the coexistence of O<sup>2−</sup>/N<sup>3−</sup> in the anion lattice. As is well established, the conduction and valence bands of simple perovskites AMX<sub>3</sub> are based mostly on the frontier orbitals of *M* and *X*, respectively. In the case of oxide perovskites, O 2*p* orbitals participate in the valence band formation near the Fermi level. However, the inclusion of nitrogen, which brings a higher 2*p* orbital energy level than that of oxygen 2*p*, can effectively shift the top of the valence band upward resulting in the decreased band gap. It is interesting to note that if the energy difference between O 2*p* (−14.1 eV) and N 2*p* (−11.4 eV) orbitals [11] is reflected onto the valence band edge positions, many of the complex oxynitrides containing Ta<sup>5+</sup>, Nb<sup>5+</sup>, or Ti<sup>4+</sup> would have band gaps falling in the visible light range (3.1–1.8 eV). Such a prospect in optical properties has motivated a number of studies on oxynitride perovskites and related phases, with views to semiconductor developments for visible light-harvesting photocatalysts or non-toxic inorganic pigments [1–8,12–18].

In 2001, Asahi et al. reported the visible light-driven photocatalytic activity of TiO<sub>2−*x*</sub>N<sub>*x*</sub> [1], which was followed by a number of studies on oxynitride-type photocatalysts. Promising photocatalysts were identified in various structure types such as simple perovskite (CaTaO<sub>2</sub>N, SrTaO<sub>2</sub>N, BaTaO<sub>2</sub>N, LaTiO<sub>2</sub>N, LaTaON<sub>2</sub>, CaNbO<sub>2</sub>N, SrNbO<sub>2</sub>N, BaNbO<sub>2</sub>N), complex perovskites (LaMg<sub>*x*</sub>Ta<sub>1−*x*</sub>O<sub>1+3*x*</sub>N<sub>2−3*x*</sub>), spinel (ZnGa<sub>2</sub>O<sub>*x*</sub>N<sub>*y*</sub>), wurtzite (Ga<sub>1−*x*</sub>Zn<sub>*x*</sub>N<sub>1−*x*</sub>O<sub>*x*</sub>), baddeleyite (TaON), and anosovite (Ta<sub>3</sub>N<sub>5</sub>) [3–6]. Among notable examples, Ga<sub>1−*x*</sub>Zn<sub>*x*</sub>N<sub>1−*x*</sub>O<sub>*x*</sub> has an absorption edge at ~500 nm and showed a quantum yield of 5.2% for 410 nm light [19]. BaTaO<sub>2</sub>N–BaZrO<sub>3</sub> solid solution could catalyze H<sub>2</sub> evolution from water without sacrificial agents [20]. TaON showed overall water splitting activity with surface modification and appropriate co-catalysts [21]. LaMg<sub>*x*</sub>Ta<sub>1−*x*</sub>O<sub>1+3*x*</sub>N<sub>2−3*x*</sub> and CaTaO<sub>2</sub>N could achieve overall water splitting with a Rh–Cr mixed oxide co-catalyst [22,23]. However, it was apparent that

the photocatalytic behavior of a particular catalyst depended not merely on the composition but the morphology, defects, co-catalysts, and the type of photocatalytic reaction.

In this study, we compare the electronic structures of several Ta<sup>5+</sup> perovskites having different anion matrices of pure oxide, oxynitride, and oxyfluoride types. The diffuse reflection absorbance spectra for ATaO<sub>2</sub>N (A = Ba, Sr, and Ca) are presented along with those of KTaO<sub>3</sub>, NaTaO<sub>3</sub>, and TaO<sub>2</sub>F, revealing a clear dependence of the semiconductor band gap on the electronegativity of anion components. The density-functional theory (DFT) based computations, combined with the valence level X-ray photoelectron spectroscopy (XPS), confirm that the N 2*p* component plays a critical role in extending the valence band edge in oxynitride compounds. We also present the photocatalytic activity of oxynitride samples tested by examining the water splitting under visible light irradiation.

## 2. Results and Discussion

Figure 1 displays the diffuse reflection absorbance spectra for simple Ta<sup>5+</sup> perovskites where the oxynitride phases are found with markedly smaller band gap energies than the others. The optical band gaps were estimated by Shapiro's method [24]. The linear region of the absorption edge was extrapolated to the wavelength axis, where the intersection (zero absorption) was taken as the band gap value. The estimated band gap energies are in the following order: BaTaO<sub>2</sub>N (1.8 eV) < SrTaO<sub>2</sub>N (2.1 eV) < CaTaO<sub>2</sub>N (2.4 eV) < KTaO<sub>3</sub> (3.6 eV) < NaTaO<sub>3</sub> (4.0 eV) < TaO<sub>2</sub>F (4.1 eV).

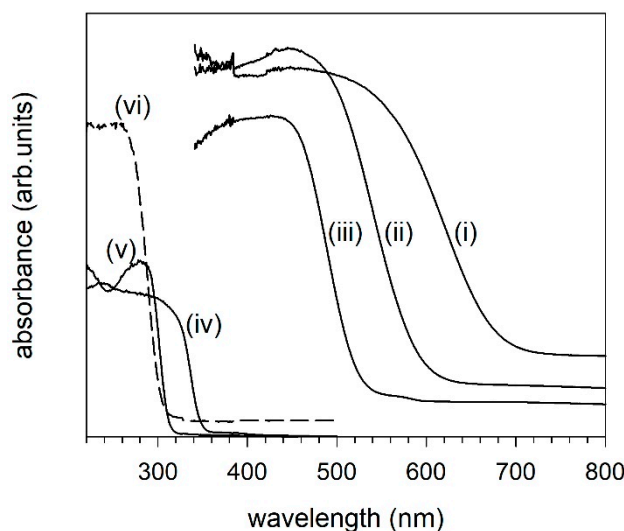


**Figure 1.** Diffuse reflection absorption spectra for (i) BaTaO<sub>2</sub>N, (ii) SrTaO<sub>2</sub>N, (iii) CaTaO<sub>2</sub>N, (iv) KTaO<sub>3</sub>, (v) NaTaO<sub>3</sub>, and (vi) TaO<sub>2</sub>F.

For the *d*<sup>0</sup> perovskites AMX<sub>3</sub>, it has been well elucidated that the band gap magnitude depends on (i) electronegativity difference between M cation and X anion, (ii) deviation of M–X–M bond angles away from 180°, (iii) M–X bond distance, and (iv) electronegativity of A cation [25,26]. The band gap variation among BaTaO<sub>2</sub>N (cubic), SrTaO<sub>2</sub>N (tetragonal), and CaTaO<sub>2</sub>N (orthorhombic) can be explained by the structural distortion factor (ii), in which the more distorted Ta–(O,N)–Ta linkage leads to the narrower band width and the wider band gap. However, the same reasoning cannot be used across distinct anion systems as the cubic KTaO<sub>3</sub> has a greater band gap than that of CaTaO<sub>2</sub>N. In this regard, it can be judged that the control of anion components among N, O, and F, which have well-separated electronegativity values, makes a dominant effect on the resulting electronic structure. The absorbance spectra were also examined by using Tauc plots [27] from which the above oxynitride perovskites were found to be indirect-gap semiconductors.

A detailed aspect of the electronic structural evolution depending on the anion components was studied by band calculations at the DFT level and the XPS measurements. Structural parameters for DFT calculations were taken from the Rietveld refinements for BaTaO<sub>2</sub>N, SrTaO<sub>2</sub>N, and CaTaO<sub>2</sub>N [10],

or from the literature data for  $\text{KTaO}_3$  [28],  $\text{NaTaO}_3$  [29], and  $\text{TaO}_2\text{F}$  [30]. Since the computation codes cannot handle mixed occupation of any crystallographic site, ordered O/N (or O/F) distributions were assumed for mixed anion phases.

The density of states (DOS) in  $\text{BaTaO}_2\text{N}$ ,  $\text{SrTaO}_2\text{N}$ ,  $\text{CaTaO}_2\text{N}$ ,  $\text{KTaO}_3$ , and  $\text{TaO}_2\text{F}$  resulted from the calculations using CAMbridge Serial Total Energy Package (CASTEP) and are compared in Figure 2. As previously observed for similar compounds, the computation tends to underestimate the band gap magnitude. Still, it can be well recognized that the width and position of valence bands vary depending on the anion components. Both of the mixed anion systems have widened valence bands due to the  $2p$  orbital mixings between O/N or O/F: extended toward a higher energy side for oxynitrides and toward a lower energy side for oxyfluoride. However, the conduction bands of those five compounds were found at fairly similar energy ranges (not shown) since they have the same octahedral cation, Ta. The net result is the effective band gap reduction in oxynitrides, as compared with oxides. On the other hand, for the oxyfluoride derivative, the band gap itself would not change very much to a first approximation.

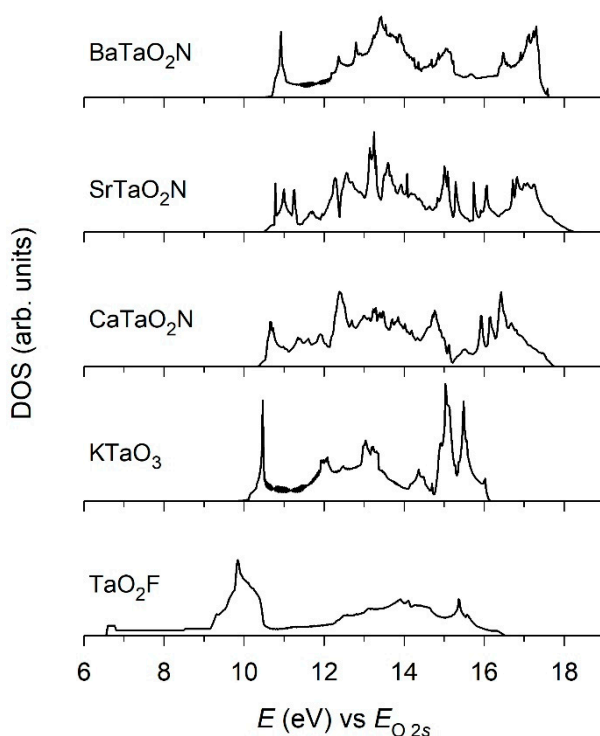


**Figure 2.** Valence band density of states (DOS) structures for  $\text{BaTaO}_2\text{N}$ ,  $\text{SrTaO}_2\text{N}$ ,  $\text{CaTaO}_2\text{N}$ ,  $\text{KTaO}_3$ , and  $\text{TaO}_2\text{F}$  as calculated using the CAMbridge Serial Total Energy Package (CASTEP) code.

The N  $2p$  contribution to band structures of oxynitride compounds can be better viewed by extracting the partial DOS of the component atoms. Figure 3 shows the DOS plots for  $\text{BaTaO}_2\text{N}$  as an example, which was obtained by employing linear muffin-tin orbital (LMTO) calculation. Both O  $p$  and N  $p$  orbitals were found as the major constituents of the valence band but notably the N character resides primarily at the upper region of the valence band, in agreement with the design concept of these oxynitride perovskites.

Along with the theoretical calculation, an experimental probe was also used to study the valence band structures of  $A\text{TaO}_2\text{N}$  ( $A = \text{Ba}, \text{Sr}, \text{Ca}$ ),  $\text{KTaO}_3$ ,  $\text{NaTaO}_3$ , and  $\text{TaO}_2\text{F}$ . The XPS spectra presented in Figure 4 were collected at near the Fermi level and, therefore, depict the DOS of valence bands. After the energy calibration using the C  $1s$  peak energy and background subtraction, the tops of the valence bands were determined as indicated on the plots (Figure 4). The valence band edges of oxynitrides were found to be higher in energy by significant margins ( $\approx 1$  eV) than the oxides' or oxyfluoride's, which is

consistent with the electronic structure calculations. It is, therefore, corroborated both experimentally and theoretically that the hybridization of O 2*p* and N 2*p* orbitals are energetically feasible in the extended solid lattice, and that the partial N/O replacement can be a useful means to reduce the band gap size of oxide semiconductors. Based on the measured band gap magnitudes and the valence band widths, simplified band structures can be proposed for the Ta<sup>5+</sup> perovskites studied here (Figure 5).

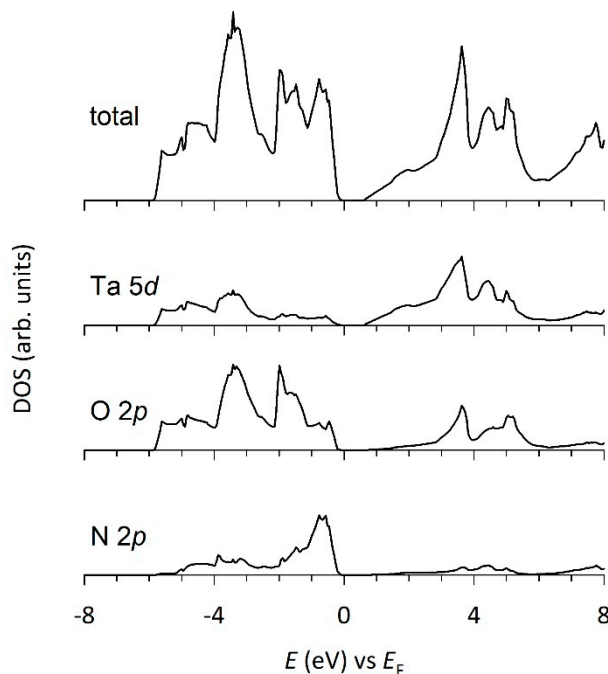


**Figure 3.** Total and partial DOS for BaTaO<sub>2</sub>N as calculated using linear muffin-tin orbital (LMTO) code.

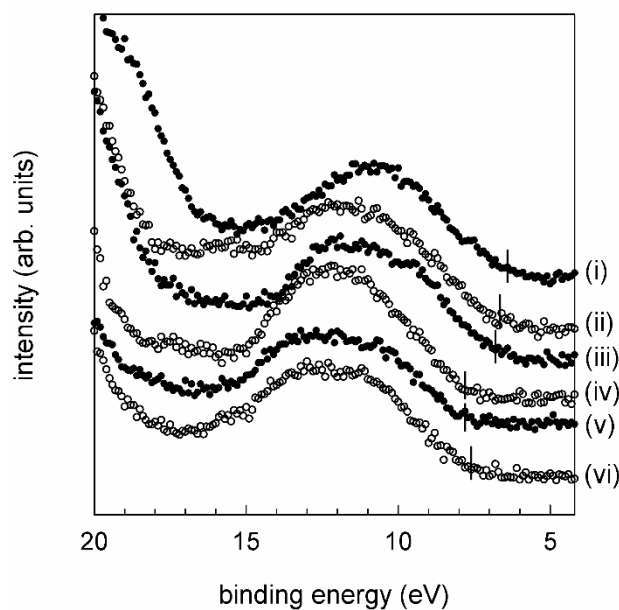


**Figure 4.** Valence level XPS spectra for (i) BaTaO<sub>2</sub>N, (ii) SrTaO<sub>2</sub>N, (iii) CaTaO<sub>2</sub>N, (iv) KTaO<sub>3</sub>, (v) NaTaO<sub>3</sub>, and (vi) TaO<sub>2</sub>F. Vertical bar on each data indicates the top edge of the valence band.

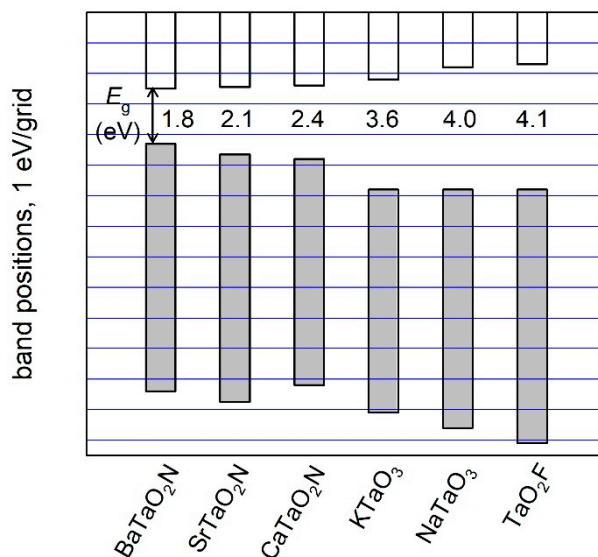


**Figure 5.** Conduction (unfilled) and valence (shaded) band positions for several simple perovskites with octahedral Ta<sup>5+</sup>, as deduced from diffuse reflection absorbance and XPS measurements.

The reduced band gaps of oxynitride phases have immediate relevance to the photocatalytic reactivity. In this respect, we tested the water splitting by Pt-loaded oxynitride samples under visible light irradiation. Figure 6 presents the time-dependent H<sub>2</sub> evolution from the Pt-CaTaO<sub>2</sub>N in H<sub>2</sub>O/CH<sub>3</sub>OH, along with the result from Pt-TiO<sub>2</sub> (P25). Since CH<sub>3</sub>OH contains carbon with a formal oxidation number of  $-2$ , it can act as a reducing agent that removes O<sub>2</sub> and expedite water decomposition as follows:



The sacrificial agent CH<sub>3</sub>OH should boost the generation of H<sub>2</sub> according to the Le Chatelier principle, and also help suppress the H<sub>2</sub>–O<sub>2</sub> recombination.

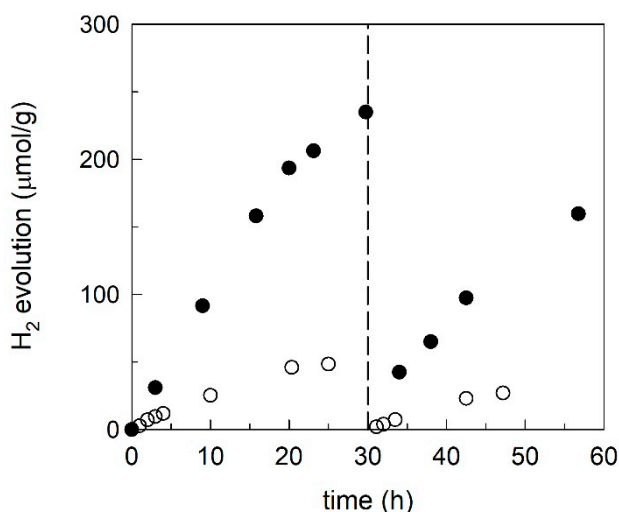


**Figure 6.** Photocatalytic H<sub>2</sub> evolutions over Pt-loaded powders of CaTaO<sub>2</sub>N (filled circles) and P25 TiO<sub>2</sub> (open circles). At the beginning and after 30 h had elapsed, the reactor vessel was purged with Ar.

As displayed in Figure 6, Pt-CaTaO<sub>2</sub>N possesses the photocatalytic activity that can be triggered by visible light photons. Using the irradiation source of  $\lambda > 395$  nm here, the photocatalytic efficiency of Pt-CaTaO<sub>2</sub>N is significantly higher than that of Pt-TiO<sub>2</sub> (P25), a well-established photocatalyst

system. Certainly, the superior performance of Pt-CaTaO<sub>2</sub>N is attributed to its narrower band gap. As can be found from Figure 1, CaTaO<sub>2</sub>N can utilize the photons with  $\lambda$  as long as  $\approx 500$  nm, whereas the absorption by TiO<sub>2</sub> (P25) is limited to  $\lambda < 400$  nm. The other oxynitride samples Pt-BaTaO<sub>2</sub>N and Pt-SrTaO<sub>2</sub>N and an oxide sample Pt-KTaO<sub>3</sub> were also examined under the same experimental condition, but none of them produced discernible amounts of H<sub>2</sub>. The lack of photocatalytic ability in Pt-KTaO<sub>3</sub> is simply ascribable to its wide band gap. However, in the cases of BaTaO<sub>2</sub>N and SrTaO<sub>2</sub>N, which possess even smaller band gap energies than CaTaO<sub>2</sub>N, the inferior photocatalytic property can be due to other factors. As one possibility, the valence band edges of BaTaO<sub>2</sub>N and SrTaO<sub>2</sub>N might be higher than the O<sup>2-</sup>/O<sub>2</sub> oxidation level, or the H<sub>2</sub>-O<sub>2</sub> recombination might occur so fast as to disallow the observation of water decomposition. Yet, BaTaO<sub>2</sub>N and SrTaO<sub>2</sub>N are regarded as promising candidates for visible light photocatalysts that could be well exploited in deliberately designed reaction systems. In the studies by Domen et al., it was demonstrated that the combination of Pt-ATaO<sub>2</sub>N (A = Ba, Sr, Ca) and Pt-WO<sub>3</sub> achieves overall water splitting under visible light in the presence of IO<sub>3</sub><sup>-</sup>/I<sup>-</sup> as a shuttle redox mediator [2,12].

### 3. Materials and Methods

#### 3.1. Sample Syntheses and Crystal Structure

Polycrystalline oxynitride samples ATaO<sub>2</sub>N (A = Ba, Sr, Ca) were prepared by ammonolysis reaction using BaCO<sub>3</sub> (J. T. Baker, 99.8%, Phillipsburg, NJ, USA), SrCO<sub>3</sub> (Aldrich, 99.9+%, St. Louis, MO, USA), CaCO<sub>3</sub> (Mallinckrodt, 99.95%, Phillipsburg, NJ, USA), and Ta<sub>2</sub>O<sub>5</sub> (Cerac, 99.5%, Milwaukee, WI, USA), as described previously [10]. Quantitative mixture of reagents was heated in anhydrous ammonia (99.99%) at a flow rate of  $\approx 50$  cm<sup>3</sup>/min. Each ammonolytic heating cycle consisted of heating/cooling ramps of 10 °C/min and a dwell step of 20 h at 1000 °C. The heat treatment cycle was repeated 2–5 times to obtain phase pure products. For preparing TaO<sub>2</sub>F, Ta powder (Alfa Aesar, 99.9%, Karlsruhe, Germany) was dissolved in HF solution (47%) in a Teflon beaker. After evaporating the solvent at 125 °C, white precipitate was washed with distilled water, dried at 150 °C, and finally heated at 500 °C in air for 1 h. Reference compounds KTaO<sub>3</sub> (Cerac, 99.9%) and NaTaO<sub>3</sub> (Cerac, 99.9%) were used as purchased.

Crystal structure analyses of ATaO<sub>2</sub>N samples used the synchrotron X-ray powder diffraction patterns collected at the beamline X7A of National Synchrotron Light Source, Brookhaven National Laboratory (Upton, NY, USA). Lattice parameters and atomic coordinates for ATaO<sub>2</sub>N phases were refined using the Rietveld method as incorporated in the GSAS-GUI software suite [31,32].

#### 3.2. Electronic Structure and Photocatalytic Property

Diffuse reflectance data were recorded and converted to absorbance using a spectrophotometer (Perkin Elmer, Lambda 20, Waltham, MA, USA) equipped with a 50-mm Labsphere integrating sphere over the spectral range 200–900 nm. The band gap energies were determined from Shapiro's method [24] of extrapolating the onset of absorption to the wavelength axis.

DFT-based computations were performed using the CASTEP program as embodied in Accelrys Materials Studio [33]. Norm-conserving nonlocal pseudo-potentials were generated using the Kerker scheme with a kinetic energy cutoff of 400 eV. A convergence criterion of 0.02 meV was applied for the energy change per atom. Electron exchange and correlation were described using the Perdew-Wang generalized gradient approximation (PW91-GGA) [34]. For BaTaO<sub>2</sub>N, the total and partial densities of states were also calculated using a computation code, Stuttgart LMTO version 47, developed by Anderson and co-workers [35,36]. The program employs a TB-LMTO-ASA (tight binding linear muffin-tin orbital atomic sphere approximation) algorithm. Integrations over  $k$  space were performed using the tetrahedron method with a total of 40 irreducible  $k$  points from a  $6 \times 6 \times 6$  grid of reducible  $k$  points.

Valence band structures of  $ATaO_2N$  ( $A = Ba, Sr, Ca$ ),  $KTaO_3$ ,  $NaTaO_3$ , and  $TaO_2F$  were experimentally studied by XPS at near Fermi energy level, using a V. G. Scientific spectrometer equipped with a  $Mg K_{\alpha}$  source (1253.6 eV) and operated at 9 kV and 20 mA with a base pressure of  $\approx 2 \times 10^{-9}$  Torr. Shirley method [37] was used for the data smoothening and background removal from the raw XPS spectra.

Photocatalytic activity of  $CaTaO_2N$ , in comparison with that of  $TiO_2$  (Degussa P25) [38], was examined for the water decomposition using visible light irradiation. To focus on the photocatalytic  $H_2$  evolution, Pt was employed as a co-catalyst [39]. For preparing the Pt-impregnated catalyst, sample powder was stirred in an aqueous solution of  $H_2PtCl_6 \cdot 6H_2O$  ( $[Pt^{4+}] \approx 0.4$  mM) under ultraviolet (UV) irradiation for 24 h, rinsed, and dried at room temperature. Thus, the obtained Pt-loaded catalyst ( $\approx 50$  mg) was suspended in a mixture of 35 mL  $H_2O$  and 0.6 mL MeOH contained in a 43.5 mL quartz vessel, which was sealed with a latex septum and filled with  $\approx 1$  atm of Ar. The photocatalytic reaction was induced by external illumination with an Oriel Xe lamp (24 V, 7 A) through a liquid filter and a long-pass filter ( $\lambda_{cutoff} = 395$  nm), and was monitored using a gas chromatograph (Shimadzu, GC-14A, Tokyo, Japan) with Ar (99.998%) carrier gas. By using the liquid filter with a circulating water cooler, the reaction vessel was kept from the heating effect of infrared light component.

#### 4. Conclusions

It was shown, using six simple perovskites with octahedral  $Ta^{5+}$ , that the semiconductor band gap can be widely modulated by the electronegativity of anion components. The band gap generally widens from oxynitrides to oxides to oxyfluorides, and in most cases, the  $d^0$  oxynitride phases have band gaps corresponding to visible light energy. Band structure calculations by the DFT method and XPS measurements indicate that the N  $2p$  component contributes to extend the top of the valence band in oxynitrides, making a principal distinction from the oxides' electronic structures. The photocatalytic  $H_2$  generation from  $H_2O$  was observed by using Pt- $CaTaO_2N$  and a sacrificial electron donor  $CH_3OH$  under visible light.

**Author Contributions:** P.M.W. designed the research and reviewed the draft. Y.-I.K. prepared and characterized the samples and wrote the draft.

**Funding:** This research was funded by the National Research Foundation of Korea (NRF-2015R1D1A1A01056591) through the Basic Science Research Program.

**Conflicts of Interest:** The authors declare no conflict of interest.

#### References

1. Asahi, R.; Morikawa, T.; Ohwaki, T.; Aoki, K.; Taga, Y. Visible-Light Photocatalysis in Nitrogen-Doped Titanium Oxides. *Science* **2001**, *293*, 269–271. [[CrossRef](#)] [[PubMed](#)]
2. Higashi, M.; Abe, R.; Takata, T.; Domen, K. Photocatalytic Overall Water Splitting under Visible Light Using  $ATaO_2N$  ( $A = Ca, Sr, Ba$ ) and  $WO_3$  in a  $IO_3^-/I^-$  Shuttle Redox Mediated System. *Chem. Mater.* **2009**, *21*, 1543–1549. [[CrossRef](#)]
3. Takata, T.; Pan, C.; Domen, K. Recent progress in oxynitride photocatalysts for visible-light-driven water splitting. *Sci. Technol. Adv. Mater.* **2015**, *16*, 033506. [[CrossRef](#)] [[PubMed](#)]
4. Wu, Y.; Lazic, P.; Hautier, G.; Persson, K.; Ceder, G. First principles high throughput screening of oxynitrides for water-splitting photocatalysts. *Energy Environ. Sci.* **2013**, *6*, 157–168. [[CrossRef](#)]
5. Zhang, P.; Zhang, J.; Gong, J. Tantalum-based semiconductors for solar water splitting. *Chem. Soc. Rev.* **2014**, *43*, 4395–4422. [[CrossRef](#)] [[PubMed](#)]
6. Ahmed, M.; Xinxin, G. A review of metal oxynitrides for photocatalysis. *Inorg. Chem. Front.* **2016**, *3*, 578–590. [[CrossRef](#)]
7. Jansen, M.; Letschert, H.P. Inorganic yellow-red pigments without toxic metals. *Nature* **2000**, *404*, 980–982. [[CrossRef](#)]
8. Tessier, F.; Marchand, R. Ternary and higher order rare-earth nitride materials: Synthesis and characterization of ionic-covalent oxynitride powders. *J. Solid State Chem.* **2003**, *171*, 143–151. [[CrossRef](#)]

9. Cabana, J.; Dupre, N.; Gillot, F.; Chadwick, A.V.; Grey, C.P.; Palacin, M.R. Synthesis, Short-Range Structure, and Electrochemical Properties of New Phases in the Li–Mn–N–O System. *Inorg. Chem.* **2009**, *48*, 5141–5153. [[CrossRef](#)]
10. Kim, Y.-I.; Woodward, P.M.; Baba-Kishi, K.Z.; Tai, C.W. Characterization of the Structural, Optical, and Dielectric Properties of Oxynitride Perovskites  $\text{AMO}_2\text{N}$  (A = Ba, Sr, Ca; M = Ta, Nb). *Chem. Mater.* **2004**, *16*, 1267–1276. [[CrossRef](#)]
11. Harrison, W.A. *Electronic Structure and the Properties of Solids*; W. H. Freeman and Company: San Francisco, CA, USA, 1980; p. 50.
12. Higashi, M.; Abe, R.; Teramura, K.; Takata, T.; Ohtani, B.; Domen, K. Two step water splitting into  $\text{H}_2$  and  $\text{O}_2$  under visible light by  $\text{ATaO}_2\text{N}$  (A = Ca, Sr, Ba) and  $\text{WO}_3$  with  $\text{IO}_3^- / \text{I}^-$  shuttle redox mediator. *Chem. Phys. Lett.* **2008**, *452*, 120–123. [[CrossRef](#)]
13. Yashima, M.; Yamada, H.; Maeda, K.; Domen, K. Experimental visualization of covalent bonds and structural disorder in a gallium zinc oxynitride photocatalyst ( $\text{Ga}_{1-x}\text{Zn}_x$ )( $\text{N}_{1-x}\text{O}_x$ ): Origin of visible light absorption. *Chem. Commun.* **2010**, *46*, 2379–2382. [[CrossRef](#)] [[PubMed](#)]
14. Hisatomi, T.; Katayama, C.; Moriya, Y.; Minegishi, T.; Katayama, M.; Nishiyama, H.; Yamada, T.; Domen, K. Photocatalytic oxygen evolution using  $\text{BaNbO}_2\text{N}$  modified with cobalt oxide under photoexcitation up to 740 nm. *Energy Environ. Sci.* **2013**, *6*, 3595–3599. [[CrossRef](#)]
15. Xiao, M.; Wang, S.; Thaweesak, S.; Luo, B.; Wang, L. Tantalum (Oxy)Nitride: Narrow Bandgap Photocatalysts for Solar Hydrogen generation. *Engineering* **2017**, *3*, 365–378. [[CrossRef](#)]
16. Mukherji, A.; Seger, B.; Lu, G.Q.; Wang, L. Nitrogen Doped  $\text{Sr}_2\text{Ta}_2\text{O}_7$  Coupled with Graphene Sheets as Photocatalysts for Increased Photocatalytic Hydrogen Production. *ACS Nano* **2011**, *5*, 3483–3492. [[CrossRef](#)] [[PubMed](#)]
17. Chen, S.; Yang, J.; Ding, C.; Li, R.; Jin, S.; Wang, D.; Han, H.; Zhang, F.; Li, C. Nitrogen-doped layered oxide  $\text{Sr}_5\text{Ta}_4\text{O}_{15-x}\text{N}_x$  for water reduction and oxidation under visible light irradiation. *J. Mater. Chem. A* **2013**, *1*, 5651–5659. [[CrossRef](#)]
18. Wang, X.; Maeda, K.; Thomas, A.; Takanabe, K.; Xin, G.; Carlsson, J.M.; Domen, K.; Antonietti, M. A metal-free polymeric photocatalyst for hydrogen production from water under visible light. *Nat. Mater.* **2009**, *8*, 76–80. [[CrossRef](#)] [[PubMed](#)]
19. Kubota, J.; Domen, K. Photocatalytic Water Splitting Using Oxynitride and Nitride Semiconductor Powders for Production of Solar Hydrogen. *Electrochem. Soc. Interface* **2013**, *22*, 57–62. [[CrossRef](#)]
20. Matoba, T.; Maeda, K.; Domen, K. Activation of  $\text{BaTaO}_2\text{N}$  photocatalyst for enhanced non-sacrificial hydrogen evolution from water under visible light by forming a solid solution with  $\text{BaZrO}_3$ . *Chem. Eur. J.* **2011**, *17*, 14731–14735. [[CrossRef](#)] [[PubMed](#)]
21. Maeda, K.; Lu, D.; Domen, K. Direct water splitting into hydrogen and oxygen under visible light by using modified TaON photocatalysts with  $d^0$  electronic configuration. *Chem. Eur. J.* **2013**, *19*, 4986–4991. [[CrossRef](#)] [[PubMed](#)]
22. Pan, C.; Takata, T.; Nakabayashi, M.; Matsumoto, T.; Shibata, N.; Ikuhara, Y.; Domen, K. A complex perovskite-type oxynitride: The first photocatalyst for water splitting operable at up to 600 nm. *Angew. Chem. Int. Ed.* **2015**, *54*, 2955–2959. [[CrossRef](#)] [[PubMed](#)]
23. Xu, J.; Pan, C.; Takata, T.; Domen, K. Photocatalytic overall water splitting on the perovskite-type transition metal oxynitride  $\text{CaTaO}_2\text{N}$  under visible light irradiation. *Chem. Commun.* **2015**, *51*, 7191–7194. [[CrossRef](#)]
24. Shapiro, I.P. Determination of the forbidden zone width from diffuse reflection spectra. *Opt. Spektroskopiya* **1958**, *4*, 256–260.
25. Cox, P.A. *The Electronic Structure and Chemistry of Solids*; Oxford University Press: Oxford, UK, 1987; pp. 45–72.
26. Eng, H.W.; Barnes, P.W.; Auer, B.M.; Woodward, P.M. Investigations of the electronic structure of  $d^0$  transition metal oxides belonging to the perovskite family. *J. Solid State Chem.* **2003**, *175*, 94–109. [[CrossRef](#)]
27. Tauc, J. Optical properties and electronic structure of amorphous Ge and Si. *Mater. Res. Bull.* **1968**, *3*, 37–46. [[CrossRef](#)]
28. Zhurova, E.A.; Ivanov, Y.; Zavodnik, V.; Tsirelson, V. Electron density and atomic displacements in  $\text{KTaO}_3$ . *Acta Cryst. B* **2000**, *56*, 594–600. [[CrossRef](#)]
29. Kennedy, B.J.; Prodjosantoso, A.K.; Howard, C.J. Powder neutron diffraction study of the high temperature phase transitions in  $\text{NaTaO}_3$ . *J. Phys. Condens. Matter* **1999**, *11*, 6319–6327. [[CrossRef](#)]
30. Frevel, L.K.; Rinn, H.W. The crystal structure of  $\text{NbO}_2\text{F}$  and  $\text{TaO}_2\text{F}$ . *Acta Cryst.* **1956**, *9*, 626–627. [[CrossRef](#)]

31. Larson, A.C.; von Dreele, R.B. *General Structure Analysis System (GSAS)—Report LAUR 86-748*; Los Alamos National Laboratory: Los Alamos, NM, USA, 1994.
32. Toby, B. *EXPGUI*, a graphical user interface for GSAS. *J. Appl. Cryst.* **2001**, *34*, 210–213. [[CrossRef](#)]
33. Segall, M.D.; Lindan, P.J.D.; Probert, M.J.; Pickard, C.J.; Hasnip, P.J.; Clark, S.J.; Payne, M.C. First-principles simulation: Ideas, illustrations and the CASTEP code. *J. Phys. Condens. Matter* **2002**, *14*, 2717–2744. [[CrossRef](#)]
34. Perdew, J.P.; Chevary, J.A.; Vosko, S.H.; Jackson, K.A.; Pederson, M.R.; Singh, D.J.; Fiolhais, C. Atoms, molecules, solids, and surfaces: Applications of the generalized gradient approximation for exchange and correlation. *Phys. Rev. B* **1992**, *46*, 6671–6687. [[CrossRef](#)]
35. Anderson, O.K.; Jepsen, O. Explicit, First-Principles Tight-Binding Theory. *Phys. Rev. Lett.* **1984**, *53*, 2571–2574. [[CrossRef](#)]
36. Anderson, O.K.; Pawłowska, Z.; Jepsen, O. Illustration of the linear-muffin-tin-orbital tight-binding representation: Compact orbitals and charge density in Si. *Phys. Rev. B* **1986**, *34*, 5253–5269. [[CrossRef](#)]
37. Shirley, D.A. High-Resolution X-Ray Photoemission Spectrum of the Valence Bands of Gold. *Phys. Rev. B* **1972**, *5*, 4709–4714. [[CrossRef](#)]
38. Ohtani, B.; Prieto-Mahaney, O.O.; Li, D.; Abe, R. What is Degussa (Evonik) P25? Crystalline composition analysis, reconstruction from isolated pure particles and photocatalytic activity test. *J. Photochem. Photobiol. A Chem.* **2010**, *216*, 179–182. [[CrossRef](#)]
39. Yang, J.Y.; Wang, D.; Han, H.; Li, C. Roles of cocatalysts in photocatalysis and photoelectrocatalysis. *Acc. Chem. Res.* **2013**, *46*, 1900–1909. [[CrossRef](#)] [[PubMed](#)]



© 2019 by the authors. Licensee MDPI, Basel, Switzerland. This article is an open access article distributed under the terms and conditions of the Creative Commons Attribution (CC BY) license (<http://creativecommons.org/licenses/by/4.0/>).